Quasi-Fixed Points and Periodic Orbits in the Zebiak–Cane ENSO Model with Applications in Kalman Filtering. Part II: Periodic Orbits

GERD BÜRGER,* STEPHEN E. ZEBIAK, AND MARK A. CANE

Lamont-Doherty Earth Observatory, Columbia University, Palisades, New York

(Manuscript received 18 August 1994, in final form 21 February 1995)

ABSTRACT

In Part II of this study on the application of the interactive Kalman filter to higher-dimensional systems, a modification suited to periodically forced systems is introduced. As in Part I, the object of study here is the ENSO model of Zebiak and Cane, but here the technique of quasi-fixed points is applied to certain Poincare maps of that system that are related to the forcing period of 1 year. As a result, it is possible to search the model systematically for possible periodic orbits, no matter whether they are stable or unstable. An unstable 4-year cycle is found in the model, and it is argued that this cycle can be traced back to a 4-year limit cycle, which is known to exist under weak atmosphere–ocean coupling. All other quasi-fixed points are related to orbits that do not appear to be periodic. The findings are applied to the modified version of the interactive Kalman filter, which deals with cycles as regimes. Comparing these results with the findings in Part I, it is found that the filter performances improve using, in the following order, the extended filter, the interactive filter with cycles, a seasonal average filter, and the original interactive Kalman filter from Part I.

1. Introduction

It has been shown in Bürger and Cane (1994) that it is possible to utilize for data assimilation purposes the tendency of nonlinear systems to occupy regimes. This was done via some modified version of the extended Kalman filter (EKF), the so-called interactive Kalman filter (IKF). In their work, Bürger and Cane deal with autonomous nonlinear systems such as the Lorenz system (see Lorenz 1963), which is a classic example of a regime-occupying system. A regime can be understood as a transient locking of the system into a quasi-linear behavior usually near an equilibrium state and, depending on the stability structure of that equilibrium, the more or less fast switching to another equilibrium. For the IKF it is, therefore, essential to know the distribution of system equilibria and which of them should be used and which not; using those with the strongest stabilities and instabilities contributes most to a good performance of the IKF. In the abstract limit that one uses every possible state as a regime, one ends up with (an infinitely more complicated version of) the EKF. But the EKF increasingly fails with higher degrees of nonlinearity and the tendency to form regimes (see Miller et al. 1994; Bürger and Cane 1994). With a suitable choice of system regimes, however, the IKF seems more appropriate to that situation, and the assimilation errors, especially during the regime switching, are drastically decreased.

The main problem for the IKF application is, hence, the determination of the system equilibria. Unlike in low-dimensional systems like that of Lorenz where one can derive the fixed points algebraically, the difficulty drastically increases when the systems become higher dimensional or, like most atmosphere and ocean systems, cannot even be described in finite dimensions by ordinary differential equations. In an effort to apply the IKF to such systems, we introduced in Part I the concept of a quasi-fixed point (QFP), see Bürger et al. (1995). QFPs have, by definition, a minimum tendency in the system's model function. (This tendency would be zero for a full fixed point.) The tendency, however, is not measured in the full space but in a certain reduced phase space that is supposed to contain, among other things, the main physical signal. The reason for this reduction lies in the fact that the determination of QFPs is done by a search algorithm that becomes unfeasible for the full system space.

As in Part I, our object of study is the El Niño–Southern Oscillation (ENSO) model of Zebiak and Cane (1987, hereafter ZC). We use the same multiple EOF projection as in Part I, with the exception that we now retain 40 multiple EOFs that explain 99% of the full system variance (as opposed to 9 EOFs and 90% variance in Part I). The reason for this will become

* Current affiliation: Potsdam Institut für Klimafolgenforschung, Potsdam, Germany.

Corresponding author address: Dr. Gerd Bürger, Potsdam Institut für Klimafolgenforschung e.V., Postfach 60 12 03, 14412 Potsdam, Germany.
E-mail: buerger@pik-potsdam.de

clear later. The main problem for the IKF application is the autonomous (time independent) character of the (quasi-)fixed points on the one hand and the nonautonomous (time dependent) character of ZC on the other. In Part I we tried to reconcile both aspects by splitting up the nonautonomous ZC into autonomous monthly pieces ZC_m and determine monthly quasi-fixed points for those models. The five QFPs we found (for each month, two cold states, two warm states, and the state of no anomalies that is a fixed point) were, from a physical point of view, not very satisfying as their existence strongly depended on the chosen phase space reduction, but they worked surprisingly well with the IKF. The filter performance was better than both a seasonal average model and the extended Kalman filter.

In Part II, we introduce an alternative to reconcile the autonomous QFPs with the nonautonomous model ZC. By switching our attention from the model tendency function to certain Poincare maps of ZC, we are able to systematically search periodic orbits of any kind. The so found orbits are of interest in their own right in understanding the dynamics of ZC (and of any model where this search can be applied). We will discuss some of the implications that this might have for the route that ZC takes toward chaotic behavior. In a final section we will apply the periodic orbits as regimes for the interactive Kalman filter, and compare the results with our findings from Part I.

2. QFPs of Poincare maps: Periodic orbits

From Part I we can assume the existence of a low-dimensional subspace of the full model space of ZC, which has the following properties:

- it contains the major part of the physical signal;
- it contains all prognostic variables for ZC.

These conditions enable us to pull each map of the full space down to the low-dimensional EOF subspace. In Part I we applied this to the single step model function ZC_m such that we could investigate the *local monthly behavior* of the model in the subspace along with its quasi-fixed points. Here we apply it to Poincare maps of the full model ZC, reflecting υ-year transitions of the model state, where υ is an integer. Their local behavior should reflect the orbit structure of the full model as it is reflected in the EOF subspace, especially periodic orbits that correspond to fixed points of the appropriate Poincare map. Symbolically, we do the following.

$$\begin{array}{ccc} z & \xrightarrow{\text{ZC } (\upsilon \text{ years})} & z' \\ \text{embedding } \Uparrow & & \Downarrow \text{ projection} \\ x & \xrightarrow[M_\upsilon]{} & x' \end{array}$$

In words, this means that for a state x in the EOF truncated phase space, $M_\upsilon(x)$ is the result of running ZC, starting from the state z that corresponds to x, for υ years and projecting the result z' back into the EOF phase space. The map $M_\upsilon: x \to x'$ represents an EOF-truncated version of the υ-year Poincare map for ZC. Similar to Part I with the function M_m, we consider the cost function

$$\Gamma_\upsilon(x) = |M_\upsilon(x) - x|. \tag{1}$$

Any periodic orbit of ZC with period υ/k years, k integer, appears as a root of $\Gamma_\upsilon(x)$. But not vice versa. The roots of Γ_υ are those orbits, which after υ years of running ZC have the same EOF projection. Not every root of Γ_υ is automatically a root of $\Gamma_{2\upsilon}$. However, the differences should disappear when we increase the EOF resolution so that, finally, υ-periodic orbits should be "visible" as roots of Γ_υ. In the Poincare map M_1 they appear as points of period υ. By applying exactly the same search algorithm as in Part I, we are therefore in a position to directly search and estimate states in the EOF space that serve as initial points x for orbits that are approximately υ periodic, depending on the size of $\Gamma_\upsilon(x)$.

As the dependence on initial conditions increases with the integration time, the dependence of Γ_υ on x increases dramatically with growing υ. Consequently, the algorithm converges much slower for large periods of υ and, in fact, fails to converge at all without a good first guess. In Part I we retained 9 multiple EOFs that explained 90% of the full system variance; for reasons which will become clear later we now keep 40 multiple EOFs that explain 99% of the variance. We confined ourselves to seek orbits γ_υ with periods $\upsilon = 1-6$ years (or fractions thereof).

3. The search algorithm

As a reference time for the Poincare map we choose mid-March. The search algorithm involves three major steps. Two of the steps deal with the estimation of a good first guess. First, we run ZC for the very long period of 40 000 years and save the mid-March conditions as reflected in the principal components $x(t)$. For any time t we calculate

$$\hat{\Gamma}_\upsilon(t) = |x(t + \upsilon \text{ yrs}) - x(t)|. \tag{2}$$

Note that because $x(t + \upsilon$ yrs) comes from an unfiltered initial condition, we generally have that $x(t + \upsilon$ yrs) $\neq M_\upsilon[x(t)]$ and so $\hat{\Gamma}(t) \neq \Gamma(t)$. But as long as the EOF resolution is fine enough, $\hat{\Gamma}_\upsilon(t)$ is a good approximate of $\Gamma_\upsilon[x(t)]$. Figure 1 depicts $\hat{\Gamma}_\upsilon(t)$ for a typical section of the run, for the periods $\upsilon = 1, \cdots, 6$ years. From the NINO3 value (lower panel), we clearly observe that active periods change with those of quiet behavior when the model evolution seems to die out; all $\hat{\Gamma}_\upsilon$ values are accordingly lower during those periods. In the active periods there is a distinct preference of the 4-yr period, as can be seen in the behavior of $\hat{\Gamma}_4$, which shows much lower values than all other periods. Picking the υ with minimum $\hat{\Gamma}_\upsilon$ for

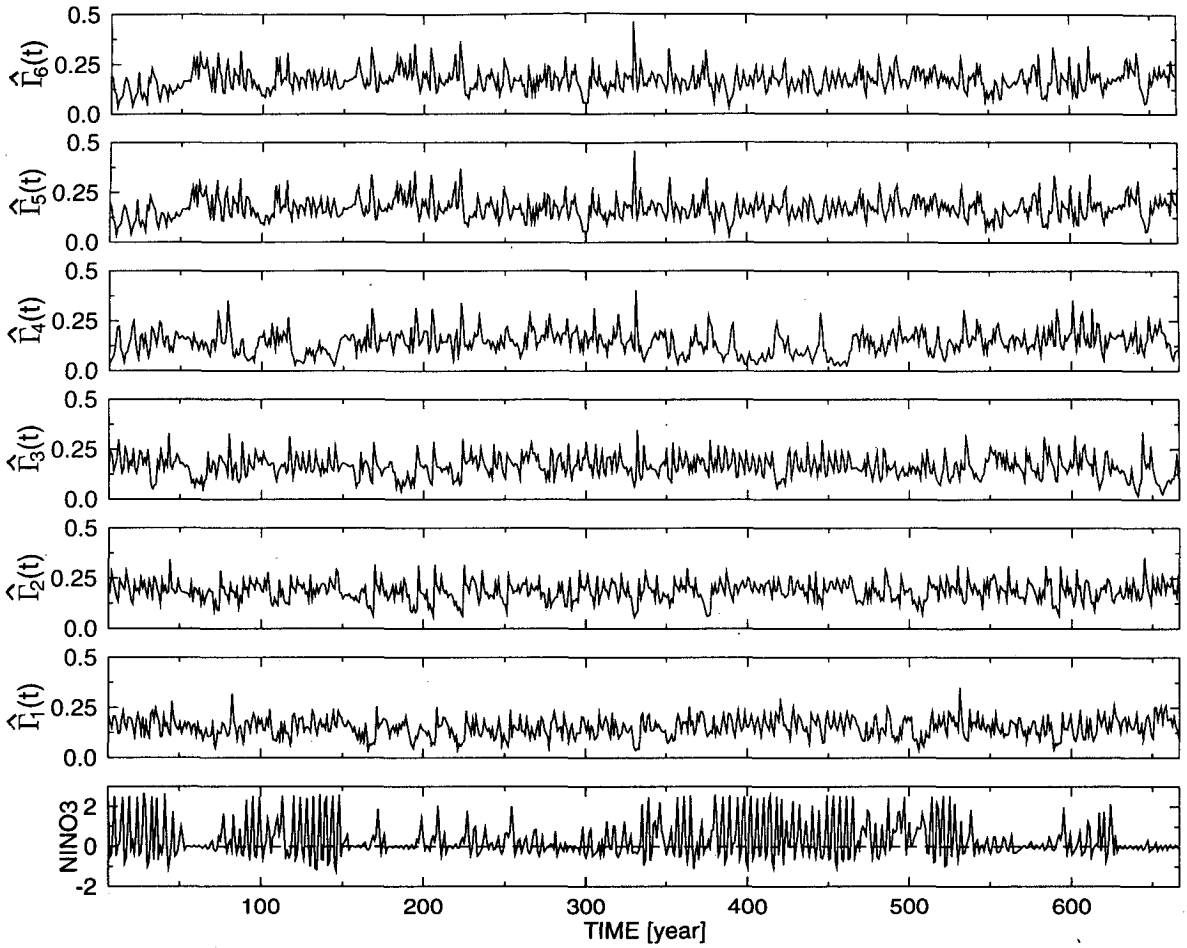

FIG. 1. The function $\hat{\Gamma}_\upsilon(t)$ for $\upsilon = 1, \cdots, 6$ (upper six panels) as calculated from the 40 000-yr run, in a typical section; we show the situation according to mid-March of each year. It measures the difference in phase space of the current state and the state υ years ahead. During active periods of the model (see lower panel) only $\hat{\Gamma}_4(t)$ shows small values over a considerable length of time. Note that $\hat{\Gamma}_2(t)$ has persistently large values then.

each t introduces a partition of the set $\{t\}$ into subsets $\{T_\upsilon\}, \upsilon = 1, \cdots, 6$; such that if $t \in T_\upsilon$, the υ periodicity is, at time t, best among all periods. A perfect υ periodic orbit would be represented in T_υ as υ points, which represent the υ different states that are taken each mid-March during the υ-year period, and its stability structure is mirrored by the cloud that surrounds each of the υ points, the blur increasing with larger instability. Figure 2 depicts the six sets of T_υ, exemplified by the scatterplot of the two leading PCs. In all periods the origin shows a certain attraction that is caused by the wandering of the system about the zero state when it is in the quiet mode. The figure suggests that there is no stable cycle of any period apart from the 1-yr period (when the system is quiet), supporting the experience with the model ZC. But especially the 4-yr period shows a strong tendency to cluster about four points in phase space, indicating that there is an unstable 4-yr cycle involved. For other periods, this is not quite as clear: in T_3 and T_5 one might recover cluster points other than the origin, but they are by far not as significant as those in T_4. An objective way to find the clustering points of the sets T_υ is to look at local maxima of the function

$$\theta_\upsilon(\xi) = \sum_{t \in T_\upsilon} e^{-[x(t)-\xi]^2/\sigma}, \tag{3}$$

which represents the density of the point clouds; σ measures the scale of the clouds. We used a standard simplex method to calculate the maxima of θ. The outcome of this search is the sought after first guess for the final estimation of the local minima of the function (1). For this minimization we applied the same conjugate gradient method that was used in Part I for the corresponding minimization problem. It uses the Levenberg–Marquardt technique for sums of real quadratic functions and calculates the Jacobian of the problem internally, see Press et al. (1992). The only thing that needs to be

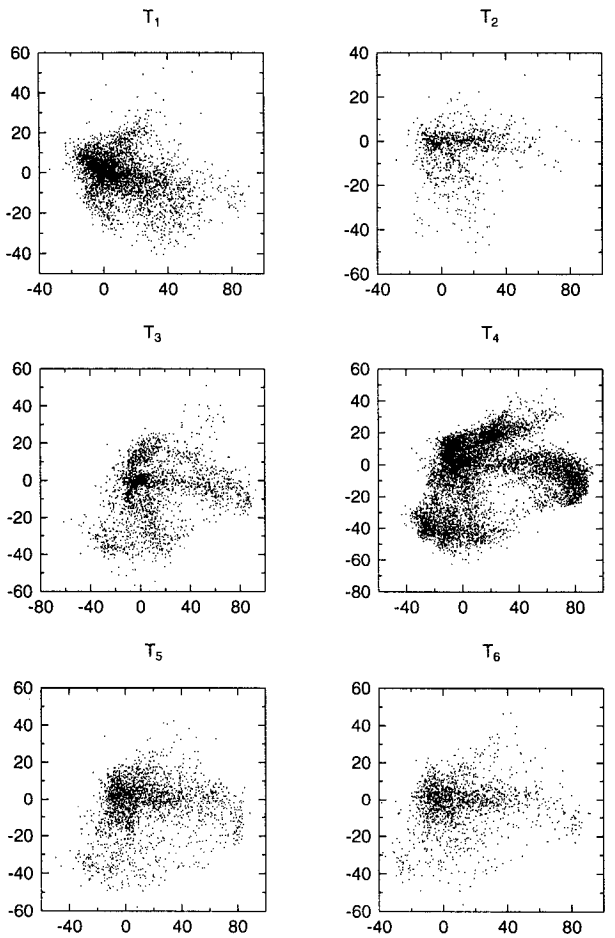

FIG. 2. The scatterplots that result from the partition of the model time steps into the six subsets T_υ, each of which consists of states $x(t)$ such that $\hat{\Gamma}_\upsilon(t)$ is a minimum among all υ. All sets together give a two-dimensional representation of the annual Poincare map of ZC. A perfectly cyclic behavior would result in a group of υ points where υ years is the period. Only T_4 shows considerable clustering. Discarding the points near the origin (they are somewhat random since they originate from the quiet model phases), one might recognize three clusters in T_3.

provided for the algorithm is the code that calculates the mapping M_υ.

4. The 4-yr cycle

The algorithm revealed the existence of a quasi-fixed point of M_4, which was very close to a true fixed point and gives strong evidence for an unstable 4-yr periodic orbit of the full model ZC. We will study this orbit now in some detail. We see in Fig. 3 the orbit, which has as initial point the QFP of Γ_4, with mean conditions taken from mid-March. We depict it in a way that demonstrates its cyclic nature, as a polar plot where the angle moves with speed 4 years per cycle and the radius shows NINO3 suitably scaled (the dashed circle is NINO3 = 0, and the origin is NINO3 = −3). As we

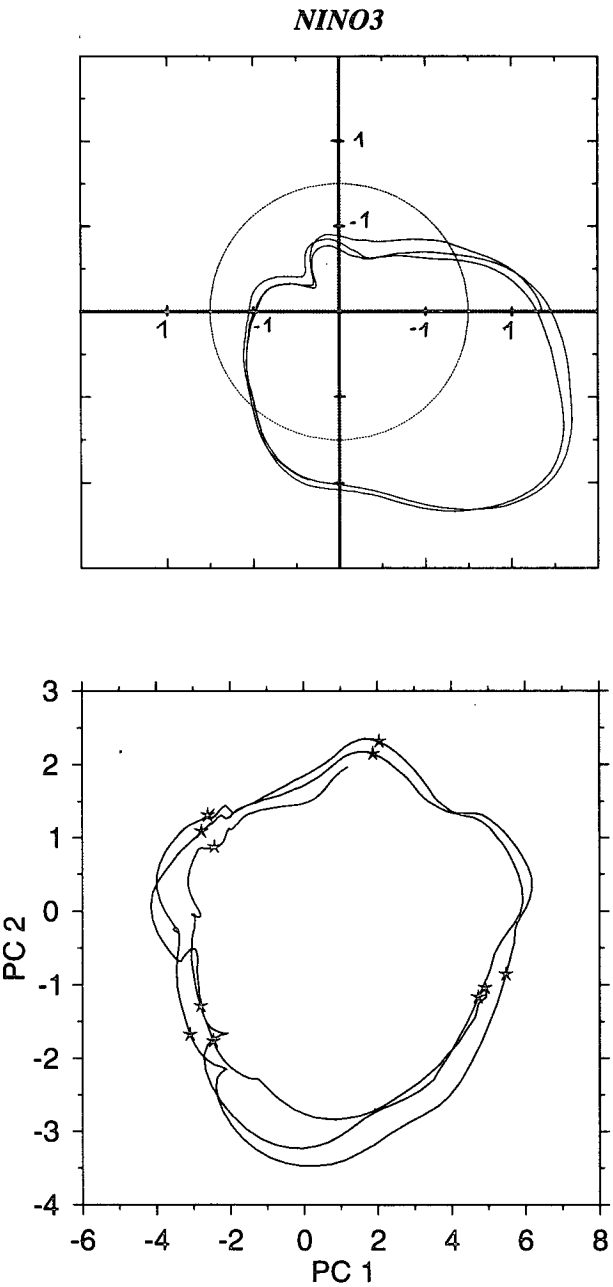

FIG. 3. The 4-yr cycle $\gamma_4(t)$, initialized from the QFP of Γ_4 in mid-March. We show NINO3 in a polar plot to emphasize the cyclic nature of $\gamma_4(t)$, and the two leading PCs. The polar angle rotates for a time period of 11 years, with speed 4 years per cycle. The radius shows NINO3 suitably scaled (the dashed circle is NINO3 = 0, and the origin is NINO3 = −3). The angle covers a period of almost 11 years. We see how, after an initialization shock, the evolution gets into an orbit that repeats itself every 4 years to a very high level of accuracy. The PC evolution where the errors between two cycles appear larger shows nevertheless the same structure within each cycle. This is marked by the stars that represent the system state of mid-March. Note the initialization shock after the first star.

started it, the NINO3 values begin, in mid-March of year 1 of the cycle, at the high level of about 2.7 and enter negative values by January of year 1 (Jan-1). A minimum NINO3 is reached by Jul-2, with minimum values of about −1.5, and after that NINO3 goes back to 0 by Jan-2. At the beginning of year 3, however, it does not turn positive but instead falls back to the negative (~ −1) during the next summer and turns positive only in the fall of year 3. The fourth year develops a strong positive anomaly of about +3.5 at Aug-4, which slowly decays to the starting values of Mar-1. From there, the next cycle is started, and we see that NINO3 evolves practically identically to its first cycle; merely in late year 7 we see minor differences of NINO3 values, but at the beginning of the third cycle they have again returned to the same values of cycles 1 and 2. At least until late year 11, the orbit is locked into the 4-yr cycle; after that it slowly diffuses to more irregular behavior.

The small deviation in Mar-2 from the initial state Mar-1 can be seen more clearly in the other panel of the figure, which depicts the two leading PCs of the orbit: the three stars at the right edge of the panel show the three states of the system at times Mar-1, Mar-2, and Mar-3. At the initial star, which corresponds to the QFP of Γ_4, we see the important detail that the system undergoes a slight initialization shock. The reason for this is that the QFP is bound to exist in a 40-dimensional subspace of the full system space, but a periodic orbit hardly projects completely onto such a subspace.

In Fig. 4 we see the 4-yr cycle as it appears in the equatorial SST, thermocline (TCL), and wind (WND) field in a Hovmöller diagram. In Mar-1, the warm pool in the east has already begun to dissipate (it culminated 3 months earlier), but the strong westerlies pile up warmer water in the east, producing a deeper thermocline there. In exchange, a negative TCL anomaly has built up in the west. By Sep-2, negative SST anomalies of moderate size spread over the entire equator, accompanied by light easterly winds. The development of a warm cell in the central Pacific by Mar-3 does not develop into a full warm phase but turns back to colder than average conditions over the full equatorial ocean. This is probably caused by the lack of warmer waters in the west, which are necessary to trigger a strong warm event. However, the renewed cold phase creates easterlies in the central Pacific that pile up new warm water in the west, and so, by Sep-3, the conditions are met that a full-scale warm event can evolve, reaching maximum positive SST anomalies of about 4.5°C by Dec-4.

Although we found strong evidence for an unstable 4-yr periodic orbit in ZC, we can never rule out with certainty that the 4-yr cycle is instead an 8-yr or 16-yr or even higher-periodic cycle; it might even be possible that what we see is the transient locking into a periodic behavior of an otherwise chaotic system (a phenomenon that is usually called intermittency). Although this question might be of some academic appeal, it is nevertheless of minor practical importance as all possibilities are not distinguishable empirically. It is known from other studies (see, e.g., Zebiak and Cane 1987; Tziperman et al. 1995) that ZC locks into a stable 4-yr cycle (limit cycle) when the parameter that controls the atmosphere–ocean coupling strength is decreased. In that case the NINO3 amplitude is much smaller than what we found here. To compare both 4-yr cycles we performed a test run of ZC with a wind stress factor (which controls the coupling) being 80% of the normal value. We do not show the result of this run, as its evolution in NINO3 and PC1/2 space, respectively, is just a scaled-down version, by a factor of about 10, of Fig. 3 (the 4-yr cycle with full coupling). We therefore conclude that it should be possible to trace the 4-yr cycle through the whole range of the coupling parameters, such that the weak, 4-yr limit cycle that governs the dynamics with little coupling gradually increases amplitude with enhanced coupling, becomes unstable, and, finally, with the normal coupling, approaches the strong, unstable 4-yr cycle.

5. Other orbits

Apart from the 4-yr cycle there is only one orbit that appears to be closely related to a periodic solution of the ZC equations. This orbit comes from the QFP of M_3 so that the period would be 3 years. But as Fig. 5 suggests the orbit appears by far not as cyclic as it does in the 4-yr case. Although the NINO3 values return to their former values from 3 years ago relatively closely, the following cycle is already so different from the first that one can hardly speak of a 3-yr periodic orbit. This becomes especially clear when we look at the two leading PCs, which differ considerably after one cycle. For the periodic orbit that might lurk behind its EOF-reduced image there is only one alternative left: it is either strongly unstable or it does not exist at all. The reason for this alternative, which applies to all other orbits as well, is that our search routine would certainly have found a stable or weakly unstable periodic orbit if there was one: with respect to the first-guess selection it is clear that a weakly unstable periodic orbit would lead to a considerable clustering in the Poincare map. And if the initialization error caused by the EOF reduction is small it cannot amplify enough to create a significant difference after one period, and this would be detected by the search algorithm. This is the reason why we wanted to keep as many EOFs as were feasible for the search algorithm (see section 2).

It has been argued recently (see Tziperman et al. 1995) that the chaotic nature of ZC is created by its capability to lock into different modes, depending on the coupling (or nonlinearity) parameters. The chaotic motion in the fully coupled case would thus be created by the system's inability to stably stay in one of these modes and to switch instead "randomly" between

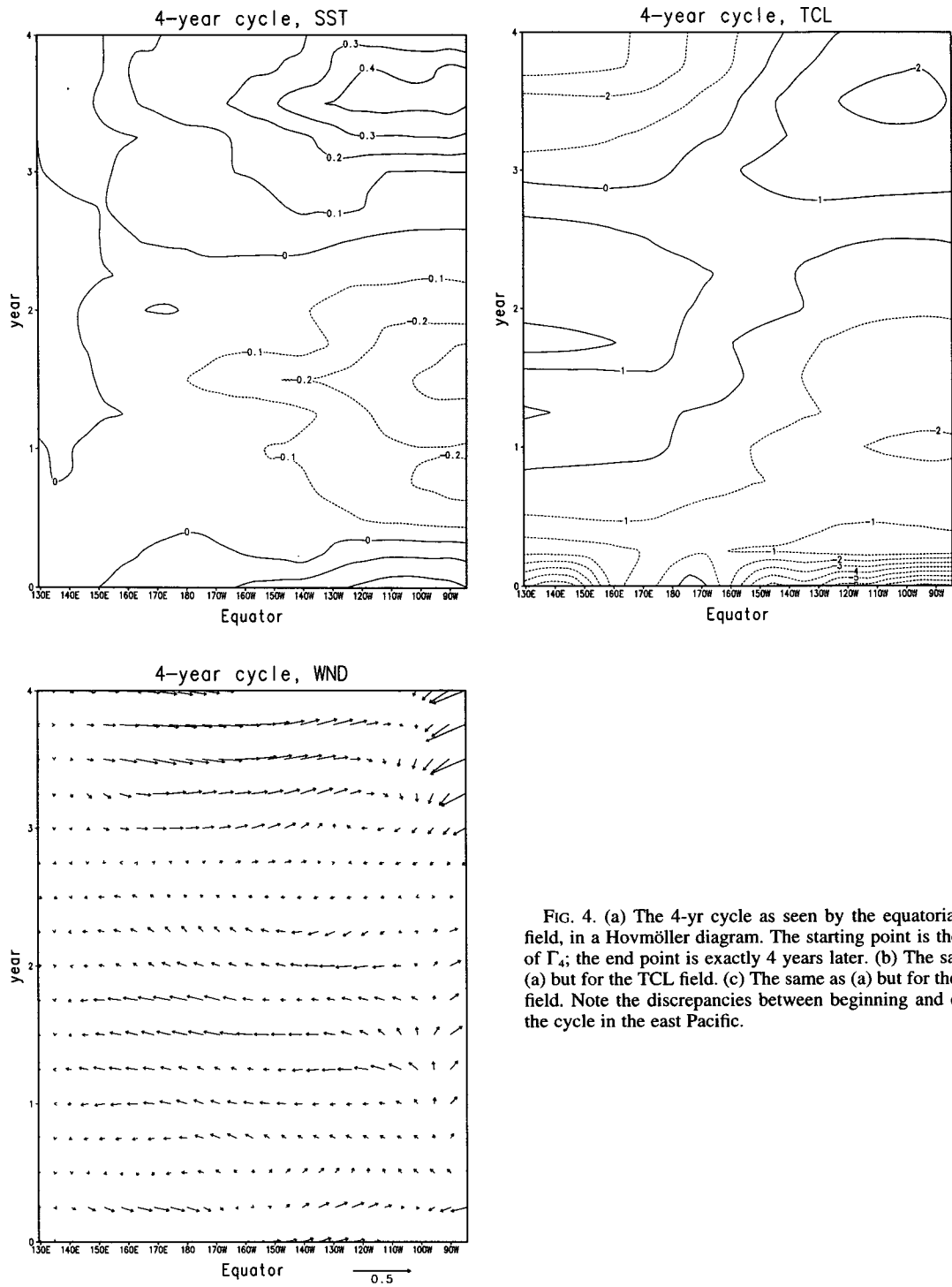

FIG. 4. (a) The 4-yr cycle as seen by the equatorial SST field, in a Hovmöller diagram. The starting point is the QFP of Γ_4; the end point is exactly 4 years later. (b) The same as (a) but for the TCL field. (c) The same as (a) but for the wind field. Note the discrepancies between beginning and end of the cycle in the east Pacific.

them. By elaborating this picture a bit further, we might say that the stability of these modes is a direct measure of their contribution to the chaotic motion. The frequency spectrum of ZC's NINO3 evolution, for example (see, e.g., Zebiak and Cane 1991), shows some power on bands other than the dominant 4-yr peak, like, for example, smaller 3-yr and 5-yr peaks. Recent studies (see Rasmusson et al. 1990; Barnett 1991; Keppenne and Ghil 1992) furthermore suggest spectral evidence for a 2-yr periodicity in the ENSO phenomenon.

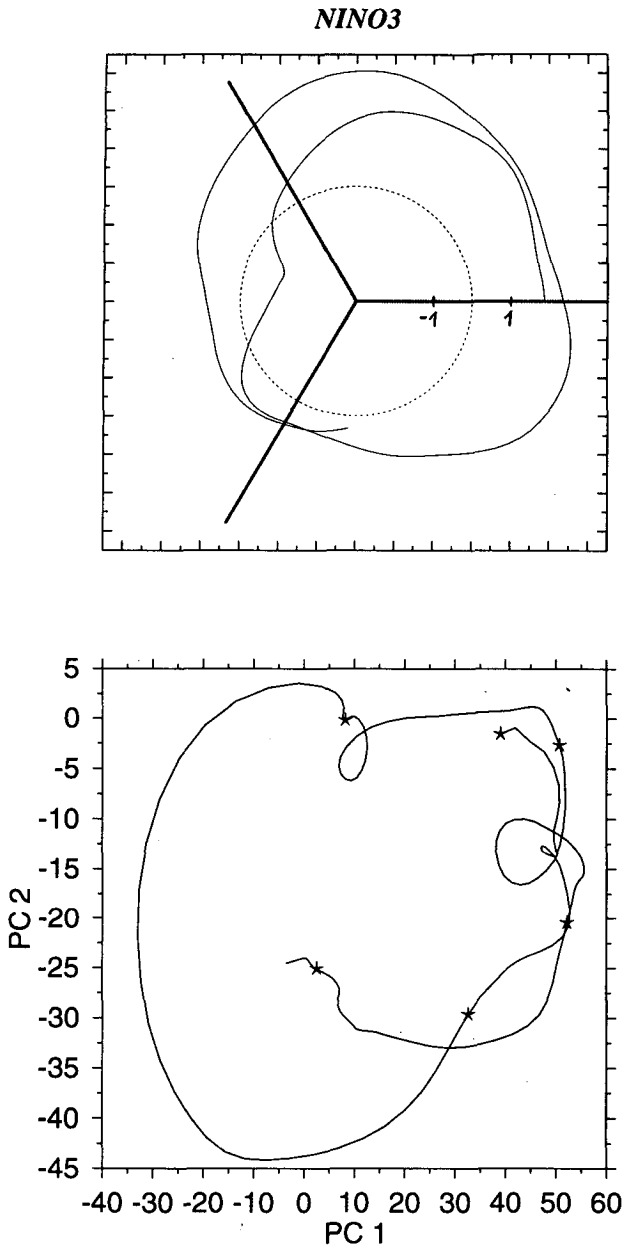

FIG. 5. Similar to Fig. 3, here for the 3-yr orbit $\gamma_3(t)$, which is the orbit initialized from the QFP of Γ_3. There is no convincing periodicity recognizable. The fact that the initial state is approached closely does not lead to periodicity.

Although the model ZC might not capture all significant ENSO periodicities, and although one should always be careful in applying linear techniques (like Fourier analysis) to nonlinear problems, there are indications that unstable cycles of periods other than 4 years exist in ZC, but they are too unstable to be detected by our routine.

As we remember, the main problem for the search algorithm, especially in the presence of strong instabilities, was the need of a good first guess. A possible method of detecting even strongly unstable cycles can be derived from the 4-yr example: there we could trace back the cycle to a limit cycle of the same characteristic that existed under weaker coupling conditions. This suggests an iterative scheme of the following kind: start with the model under weak coupling and determine the (possibly) stable cycles. Use those as initial guesses for a new search under slightly enhanced coupling strength, and so forth until the full coupling case. But this can be only the topic of another study.

As mentioned earlier, there is no chance of finding an exact periodic orbit in any of the reduced spaces we consider, and thus there will always be some initial error in the search algorithm. This fact, together with the growth of any initial error as described in Part I of this study, enforces that after already one or two cycles the initial error has grown to a size comparable to the process itself. This causes the gradient of the cost function to be extremely hard to estimate. A refined calculation of the gradient such as via the adjoint model might bring significant progress in this case.

6. Interactive Kalman filtering using the cycles

Although the 3-yr orbit did not show clear periodic behavior, we decided to include it, together with the 4-yr cycle and the cycle of no anomalies (which is a 1-yr cycle), for assimilation experiments with the interactive Kalman filter. For this, a slight modification of this filter, together with a reinterpretation of what we understand as a regime, is necessary.

The basic concept used by the interactive Kalman filter, the regime, was understood so far to be a time-independent, quasi-linear behavior that is occupied by the system for a while until it *switches,* more or less quickly, to another regime. The quasi-linear behavior of a regime usually comes from a nearby fixed point or equilibrium, and the dynamics are those of the fixed point's localization. In this way, the global behavior of the system can be understood as a sequence of regime lockings interrupted by sharp and therefore highly nonlinear switches between the regimes.

What has been a time-independent quasi-linear behavior will now become a time-dependent periodic behavior. In other words, we want to deal with systems whose global behavior can be understood as a sequence of transient lockings into different cycles, as described in the former section. We will refer to the cycle-version of the interactive Kalman filter as IKF_c. To apply the IKF_c we need a *weighting function* of the cycles that reflects this locking. Consequently, the only change for the IKF_c comes through a different definition of the weighting; all other elements of the filter are exactly like in Part I, and we refer the reader to that part. In the appendix we give a detailed definition of the weighting function. Here we need to know only the following: for a number of periodic solutions (cycles)

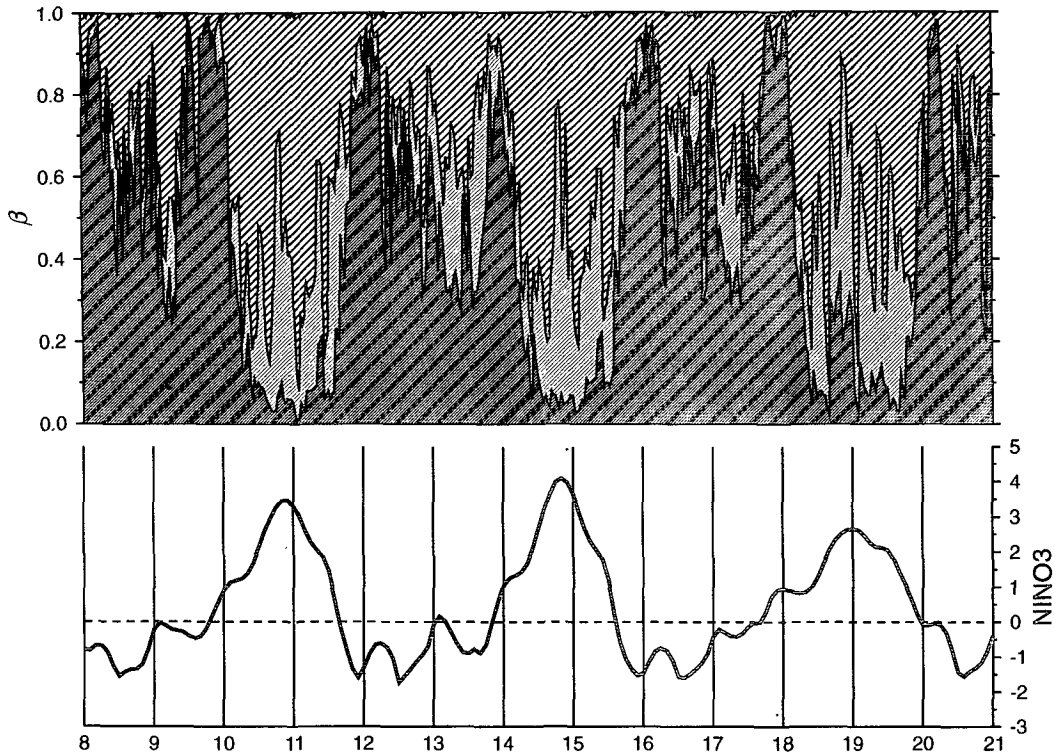

FIG. 6. The weighting β (upper panel) of the 3 cycles $\gamma_1(t)$ (hatched), $\gamma_3(t)$ (gray), and $\gamma_4(t)$ (dark gray) cumulatively, calculated from a run of ZC with typical NINO3 evolution (lower panel). There is no clear sign of a persistent cycle regime over a time span longer than the duration of that cycle. The warm and cold events are governed by the 4-yr cycle $\gamma_4(t)$, and the transitions between them by the no-anomaly cycle $\gamma_1(t)$. The 3-yr cycle $\gamma_3(t)$ is of minor importance; only the peak warm phases seem to be governed by it.

$\gamma_i(t)$, $i \leq N$, of ZC, we can assign to each state of ZC N numbers β_i, $i \leq N$, such that

- $0 \leq \beta_i \leq 1$;
- $\Sigma \beta_i = 1$; and
- γ_i is a good approximation of ZC $\Rightarrow \beta_i \to 1$.

In Part I we performed assimilation experiments with three different Kalman filters: a seasonal filter whose error model is determined by a monthly Markov transition matrix; the interactive Kalman filter with regimes chosen from the monthly quasi-fixed points; and the extended Kalman filter whose error model is given by the local linearization of the current state of the (assimilated) system. To be able to compare our results with Part I, all assimilations were done in the truncated phase space defined by the nine leading EOFs of the multiple EOF projection, which represent 90% of the entire model variance. The true process was a ZC run, and observations were generated synthetically by perturbing this run with a white noise process, the variance of which is given by the variance of the true process (in the reduced space), scaled by some factor ψ, which varied between 0 and 1.

To exemplify the behavior of the weighting function, we depict in Fig. 6 a section of the weighting that has been applied to the *true* process of one of the assimilation test runs. We used the 1-yr (no anomalies, β_1), 3-yr (β_3), and the 4-yr (β_4) cycle that are described above. As a comparison, we also show the true process in terms of NINO3. We clearly see the minor role of the 3-yr cycle, although it gains some weight during peak phases of NINO3. But the main feature is that β_4 does not become dominant for longer than a fraction of the basic period of 4 years. The cycle γ_4 seems to dominate the warm and cold peak phases for about 1.5–2 years, but each time the temperature sign changes γ_1 becomes dominant for about half a year. We have to conclude that, either, our choice of the weighting function is not appropriate, or, the model ZC does not settle into a periodic behavior over a significant time span that at least covers that period.

Under the same conditions as in Part I, we performed a number of assimilation runs with various observational noise scales ψ. Figure 7 depicts, in a typical section for the scale $\psi = 0.6$, the outcome of the assimilation together with the three filters of Part I. We show the filter's sensitivity to observations as well as the assimilation error (both defined in Part I, see the appendix) together with the true NINO3 index. Compared to the other three filters, the IKF_c lies between the EKF

and the seasonal filter. This can be seen especially during strong events when the EKF error peaks and has the lowest sensitivity toward observations. The IKF_c error also rises strongly in the beginning of an event but then drops earlier than the EKF error. The reason for this can be found in the sensitivity that grows back to normal values in the middle of an event. Although β_3 is strong in the peak phase of an event, we attribute this sensitivity growth to the instabilities of the origin because β_1 becomes stronger right after an event. Table 1 shows the performance result of all four filters. Note that because observations are available only every third time step, Δ goes beyond 100%. For small noise levels (ψ = 0.2–0.6) the IKF performs better than all other filters; the other filters are similar, with errors that are about 30% larger. For ψ = 1.0, the seasonal filter and the IKF_c are similarly good compared to the other two.

TABLE 1. The overall performance of the four Kalman filters (we adopt the measure Δ from Part I; SEAS denotes the seasonal average filter). Columns give the various noise levels Ψ. For smaller noise (Ψ = 0.2–0.6) the IKF shows the smallest assimilation error. For Ψ = 1.0, both the IKF and the EKF show similar errors slightly larger than the other two, which are also similar.

Δ (%)	SEAS	IKF	IKF_C	EKF
0.2	166.2	137.2	168.3	165.1
0.4	100.1	88.6	102.8	102.2
0.6	69.8	66.2	71.0	72.8
0.8	53.0	54.5	53.6	57.9
1.0	42.7	47.6	42.8	46.8

7. Conclusions

In a second approach to utilize regimes for the purpose of data assimilation, we undertook in this study an approach via periodic orbits. Compared to Part I, this approach seems more physical and more appropriate for a periodically forced system like the Zebiak–Cane model ZC. Both parts are linked through the notion of a quasi-fixed point: This is defined to be a state, in a suitably defined subspace of the model space, where the system's tendency is at a minimum. For a fixed point, this minimum would be zero, and the smaller the minimum the more a quasi-fixed point should share the merits of a full fixed point (mainly the

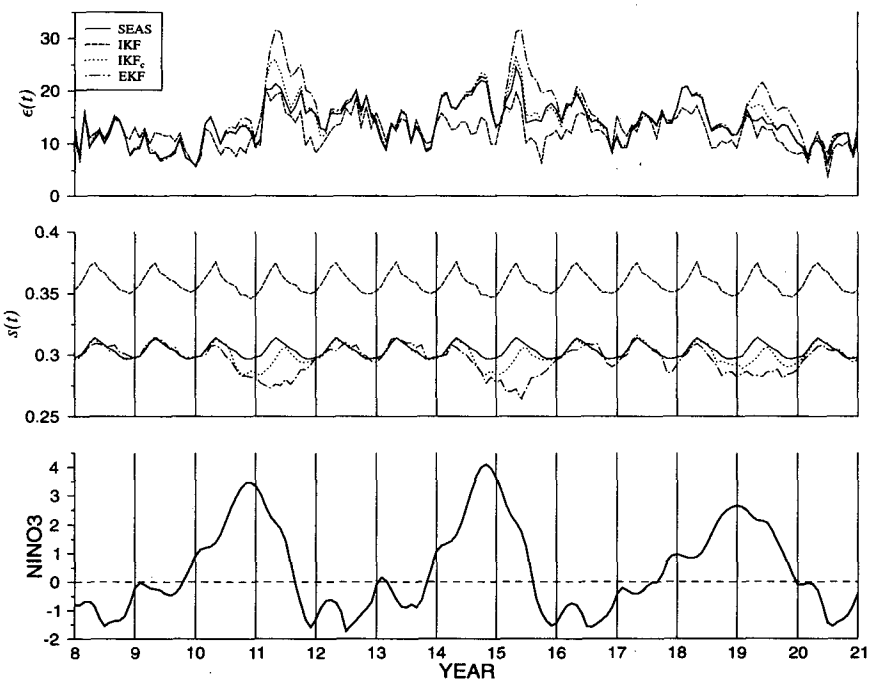

FIG. 7. Assimilation result from a typical section of a ZC run by using the four Kalman filters SEAS (the seasonal average filter, solid lines), IKF (using the quasi-fixed points from Part I as regimes, dashed lines), IKF_c [using the three cycles $\gamma_1(t)$, $\gamma_3(t)$, $\gamma_4(t)$ as regimes, dotted lines], and the EKF (dash–dot lines). (lower panel) The true NINO3 values. (middle panel) The sensitivity function. Note the drops of sensitivity for the IKF_c and EKF during warm events. The IKF_c sensitivity returns to the normal values earlier than the EKF sensitivity. The other two sensitivity functions show just the typical seasonality (more sensitive in spring and less in fall), but the IKF_c function is much greater. (upper panel) The error functions. Generally, the IKF error has the lowest values of all. Especially during the breakdown of warm events (years 11 and 15) the EKF (and IKF_c) error is drastically increased. Similarly, during fast warmings (year 14) the IKF error remains low, unlike the other filters.

richness of the local structure). The advantage of quasi-fixed points is that they can be determined purely numerically, by an application of standard search algorithms that find local minima of multidimensional functions. But before we can utilize quasi-fixed points as regimes for ZC, we have to find a way to reconcile the autonomous (time independent) nature of quasi-fixed points with the nonautonomous (time dependent) character of ZC. In Part I we did this by splitting up ZC into its monthly autonomous pieces ZC_m and determined quasi-fixed points for these. As it turned out, the so designed interactive Kalman filter appeared superior to both a seasonal average filter as well as the standard extended Kalman filter.

Although the monthly quasi-fixed points are valuable from a pragmatic point of view, they seem unsatisfactory from a physical perspective as, for instance, their existence heavily depends on the chosen reduction. In the current study (Part II), we have tried an approach that is more satisfying from a physical standpoint but, as it turned out, is less practically useful, at least for data assimilation purposes. By interpreting quasi-fixed points not for the monthly pieces ZC_m but, instead, for the Poincare maps of the various periods, we were able to systematically search for periodic orbits and apply the solutions as regimes for the interactive Kalman filter. The definition of a regime as the transient locking of a system into periodic behavior is, as far as ZC is concerned, physically intuitive and echoes current interpretations of that system's chaotic nature. The method of how to weigh the regimes for a single state of the system is chosen similarly to the method used in Part I. It reflects the quality of the approximation of the current dynamics by the single regimes.

Our search algorithm revealed, apart from the ever-present (1 yr) cycle of no anomalies, an unstable 4-yr cycle, which we can trace back to the well-known stable solution in the case of weak atmosphere–ocean coupling. No other convincing quasi-fixed points—that is, cycles—were found. This is probably caused by the fact that the search routine is unable to detect strongly unstable periodic orbits. We suspect, however, that such orbits can be detected by utilizing the models mode-locking behavior under weaker coupling conditions. A full overview of all stable or unstable periodic orbits would certainly provide valuable insight into the nonlinear dynamics of the model, especially as its route to chaotic behavior is concerned.

In the most practical sense, the cycles we just described are not very useful—at least not how we used them for the interactive Kalman filter IKF_c. Our simulations showed that although the IKF_c worked slightly better than the extended filter both the seasonal average filter and the IKF, as they are described in Part I, showed much smaller assimilation errors. The reason can be found in the different behavior of the filter sensitivity toward observations. During fast system changes, like when an El Niño event is generated or during the breakdown of such an event, the assimilation error for both the EKF and the IKF_c increases drastically. We can attribute this to the fact that the filter listens too little to observational input during those "switches," a characteristic that occurs similarly in other highly nonlinear systems such as the Lorenz system. From that system we learned earlier that it is the strong stability–instability structure about its fixed points that can significantly contribute to the evolution of the error model, by flexibly decreasing or increasing the estimated assimilation error covariance or sensitivity, respectively. We see this same mechanism working again for the IKF_c, when in the middle of an event the error goes down and the sensitivity goes up parallel to the contribution of the 1-yr cycle, the fixed point of no anomalies. Nevertheless, from our results from Part I we have to conclude that this mechanism works much more effectively with the original IKF or even the seasonal filter. A possible improvement might come from the inclusion of more unstable periodic orbits if they exist, as they would provide faster error growth in the assimilation.

With similar arguments one can explain the generally higher level of sensitivity toward observational input: With only a few of very unstable regimes being constantly active during the assimilation (through the weighting) and not only when the state actually passes through them (like in the EKF), the general influx of instability into the error model is increased, and so is the sensitivity.

The question of how applicable the IKF or IKF_c is for assimilation purposes with real data can generally be reduced to the possibility of working in an EOF reduced space at all. If one finds a method of projecting the error structure of ZC, say, to a reduced space, one should be able to apply the interactive Kalman filter. In this direction much effort has been undertaken with considerable success. The next step will, therefore, be to combine the reduction method with the application of the IKF (or, if one wants, the IKF_c) and its quasi-fixed points to see if a significant improvement can be achieved.

APPENDIX

The Modified Interactive Kalman Filter Weights

We assume that the system S under consideration is given by

$$x(t) = f[x(t-1), t], \tag{A1}$$

where $x(t)$ denotes the state of the system and the dependence of the model function f on the time t is periodic with period P. For simplicity, we assume that P equals 1 year, but it could as well be 1 day, 0.5 years, or any other period. We further assume that we have N periodic solutions (cycles) $\gamma_i(t)$, $i \leq N$, with periods

$P_1, \ldots, P_N$, which are multiples of 1 year. We further consider the Jacobian ∇f to be known at each month of each cycle γ_i. The definition of the weighting proceeds in two steps.

Given a state $x(t)$ that S occupies in March, say, we find, for each cycle γ_i a number P_i of March situations, $\gamma_i(t_1), \ldots, \gamma_i(t_{P_i})$. Writing, for each $j \leq P_i$,

$$x(t) = \gamma_i(t_j) + \xi_j(t), \tag{A2}$$

we can calculate the differences

$$\delta_j^0 = \|f[\gamma_i(t_j)] + \nabla f_{x=\gamma_i(t_j)}\xi_j(t) - f(x)\| \tag{A3}$$

and let

$$\delta_i(t) = \min_{j \leq P_i} \delta_j^0. \tag{A4}$$

This is a formal way of expressing the goal to use the March situation of each cycle that gives the best current approximation to the actual state and dynamics of S. The weighting itself can now be given as

$$\beta_i(t) = \frac{1/\delta_i^2(t)}{\sum_{j \leq N} 1/\delta_j^2(t)}, \tag{A5}$$

which is the same expression that has been used for the time-independent version of the interactive Kalman filter. As time enters April, the same is done for that month.

Three quantities are of importance for any assimilation. The two time series of the assimilation error itself,

$$\epsilon(t) = |\tilde{x}(t) - x(t)|, \tag{A6}$$

where $\tilde{x}(t)$ is the assimilated value, and the sensitivity of the assimilation toward observations

$$s(t) = \sum_{i \leq N} \left[\sum_{j \leq n} (\mathbf{K}_t)_{ij}^2 \right]^{1/2}, \tag{A7}$$

with $\mathbf{K}_t$ being the Kalman gain matrix; with the actual assimilation error covariance $\mathbf{P}$ and the observational noise $\mathbf{R}$ one can define the performance index $\Delta = \mathrm{Tr}(\mathbf{P})/\mathrm{Tr}(\mathbf{R})$, which is a good measure for the overall performance of the assimilation.

REFERENCES

Barnett, T. P., 1991: The interaction of multiple time scales in the tropical climate system. *J. Climate,* **4,** 269–285.

Bürger, G., and M. Cane, 1994: Interactive Kalman filtering. *J. Geophys. Res.,* **99**(C4), 8015–8031.

——, S. E. Zebiak, and M. A. Cane, 1995: Quasi-fixed points and periodic orbits of the Zebiak–Cane ENSO model with applications in Kalman filtering. Part I: Monthly quasi-fixed points. *Mon. Wea. Rev.,* **123,** 2802–2813.

Keppenne, C., and M. Ghil, 1992: Adaptive filtering and the prediction of the Southern Oscillation index. *J. Geophys. Res.,* **97,** 20 449–20 454.

Lorenz, E., 1963: Deterministic nonperiodic flow. *J. Atmos. Sci.,* **20,** 130–141.

Miller, R., M. Ghil, and F. Gauthier, 1994: Advanced data assimilation in strongly nonlinear dynamical systems. *J. Atmos. Sci.,* **51,** 1037–1056.

Press, W. H., S. A. Teukolsky, W. T. Vetterling, and B. P. Flannery, 1992: *Numerical Recipes in C.* Cambridge University Press.

Rasmuson, E. M., X. Wang, and C. F. Ropelewski, 1990: The biennial component of ENSO variability. *J. Mar. Syst.,* **1,** 71–96.

Tziperman, E., M. A. Cane, and S. E. Zebiak, 1995: Irregularity and locking to the seasonal cycle in an ENSO prediction model as explained by the quasi-periodicity route to chaos. *J. Atmos. Sci.,* **52,** 293–306.

Zebiak, S., and M. Cane, 1987: A model El Niño–Southern Oscillation. *Mon. Wea. Rev.,* **115,** 2662–2678.

——, and ——, 1991: Natural climate variability in a coupled model. *Greenhouse-Gas Induced Climate Change: A Critical Appraisal of Simulations and Observations.* Elsevier, 457–469.